Icarus 204 (2009) 443–457

Contents lists available at ScienceDirect

Icarus

journal homepage: www.elsevier.com/locate/icarus

Subsurface structure of Planum Boreum from Mars Reconnaissance Orbiter Shallow Radar soundings

Nathaniel E. Putzig [a,*], Roger J. Phillips [a,b], Bruce A. Campbell [c], John W. Holt [d], Jeffrey J. Plaut [e], Lynn M. Carter [c], Anthony F. Egan [a], Fabrizio Bernardini [f], Ali Safaeinili [e,1], Roberto Seu [g]

[a] Southwest Research Institute, Boulder, CO 80302, USA
[b] Washington University, St. Louis, MO 63130, USA
[c] Center for Earth and Planetary Studies, Smithsonian Institution, Washington, DC 20013, USA
[d] Jackson School of Geosciences, University of Texas, Austin, TX 78712, USA
[e] Jet Propulsion Laboratory, California Institute of Technology, Pasadena, CA 91109, USA
[f] A&C2000 s.r.l., Viale Cristoforo Colombo 436, 00145 Rome, Italy
[g] Dipartimento InfoCom, Università di Roma "La Sapienza," I-00184 Rome, Italy

ARTICLE INFO

Article history:
Received 27 April 2009
Revised 22 July 2009
Accepted 22 July 2009
Available online 30 July 2009

This article is dedicated to the memory of Ali Safaeinili, 1964–2009. Dr. Safaeinili was a key contributor to the design and operation of planetary radars and served as the SHARAD Instrument Scientist.

Keywords:
Mars
Radar observations
Mars, Polar caps
Mars, Polar geology

ABSTRACT

We map the subsurface structure of Planum Boreum using sounding data from the Shallow Radar (SHARAD) instrument onboard the Mars Reconnaissance Orbiter. Radar coverage throughout the 1,000,000-km^2 area reveals widespread reflections from basal and internal interfaces of the north polar layered deposits (NPLD). A dome-shaped zone of diffuse reflectivity up to 12 μs (~1-km thick) underlies two-thirds of the NPLD, predominantly in the main lobe but also extending into the Gemina Lingula lobe across Chasma Boreale. We equate this zone with a basal unit identified in image data as Amazonian sand-rich layered deposits [Byrne, S., Murray, B.C., 2002. J. Geophys. Res. 107, 5044, 12 pp. doi:10.1029/2001JE001615; Fishbaugh, K.E., Head, J.W., 2005. Icarus 174, 444–474; Tanaka, K.L., Rodriguez, J.A.P., Skinner, J.A., Bourke, M.C., Fortezzo, C.M., Herkenhoff, K.E., Kolb, E.J., Okubo, C.H., 2008. Icarus 196, 318–358]. Elsewhere, the NPLD base is remarkably flat-lying and co-planar with the exposed surface of the surrounding Vastitas Borealis materials. Within the NPLD, we delineate and map four units based on the radar-layer packets of Phillips et al. [Phillips, R.J., and 26 colleagues, 2008. Science 320, 1182–1185] that extend throughout the deposits and a fifth unit confined to eastern Gemina Lingula. We estimate the volume of each internal unit and of the entire NPLD stack (821,000 km^3), exclusive of the basal unit. Correlation of these units to models of insolation cycles and polar deposition [Laskar, J., Levrard, B., Mustard, J.F., 2002. Nature 419, 375–377; Levrard, B., Forget, F., Montmessin, F., Laskar, J., 2007. J. Geophys. Res. 112, E06012, 18 pp. doi:10.1029/2006JE002772] is consistent with the 4.2-Ma age of the oldest preserved NPLD obtained by Levrard et al. [Levrard, B., Forget, F., Montmessin, F., Laskar, J., 2007. J. Geophys. Res. 112, E06012, 18 pp. doi:10.1029/2006JE002772]. We suggest a dominant layering mechanism of dust–content variation during accumulation rather than one of lag production during periods of sublimation.

1. Introduction

Sounding-radar instruments in orbit around Mars (Picardi et al., 2005; Seu et al., 2007b) are yielding a wealth of subsurface data, especially from the polar regions, where icy layered deposits extend to depths of several kilometers (Plaut et al., 2007; Seu et al., 2007a; Phillips et al., 2008). Here, we describe radar mapping of the subsurface structure of ice-rich layers in Planum Boreum, at the north pole of Mars. The geometry of the radar reflectors and their correspondence with layered units observed in surface images are key to assessing the geologic history of the layers and to evaluating their implications for the past and present climate of Mars (e.g., Fishbaugh and Head, 2005; Phillips et al., 2008; Milkovich et al., 2009), much as they are for Earth (e.g., Morse et al., 1998; Welch and Jacobel, 2003).

The most prominent features in the polar regions of Mars are stacks of finely layered materials up to ~4-km thick that are nearly centered on each pole and are cut by large, arcuate chasmata and smaller reentrant and interior troughs. These materials are composed primarily of water ice with a variable amount of lithic inclusions (Picardi et al., 2005; Plaut et al., 2007), whose contrast with ice reveals the layered nature of the deposits in optical images, both on the periphery and within the chasmata where surface

* Corresponding author. Address: Southwest Research Institute, 1050 Walnut Street, Suite 300, Boulder, CO 80302, USA. Fax: +1 303 546 9687.
E-mail address: nathaniel@putzig.com (N.E. Putzig).
[1] Deceased.

0019-1035/$ - see front matter © 2009 Elsevier Inc. All rights reserved.
doi:10.1016/j.icarus.2009.07.034

exposures occur (Clifford et al., 2000, and references therein. See, however, Herkenhoff et al., 2007, who suggest that the apparent brightness of layers is controlled more by topography, texture, and surficial frosts than by internal composition). High-resolution images of Planum Boreum indicate that a major division exists between the upper stack of layered deposits (referred to hereinafter as the "NPLD") and a lower basal unit (BU), where the lower unit is typically darker and its layers less continuous (Byrne and Murray, 2002; Fishbaugh and Head, 2005). From the image data, the BU is inferred to extend beneath most of the main lobe of the polar cap but generally not beneath the Gemina Lingula lobe (Fig. 1). This inference led Fishbaugh and Head (2005) to suggest that the location of Chasma Boreale (Fig. 1) may have been controlled by that of the BU. On the basis of morphological differences, Tanaka et al. (2008) subdivide the BU into the Rupes Tenuis unit, a terraced lower sequence interpreted to be of Early Amazonian age, and the Planum Boreum *cavi* unit, a more resistant upper sequence interpreted to be of middle to late Amazonian age. We see no features in the radar data that would allow differentiation of these geologic units, so we use the collective term "basal unit" or "BU" when referring to these materials. "Planum Boreum" refers to the polar-plateau landform, which consists of the BU and the NPLD.

The Mars Advanced Radar for Subsurface and Ionospheric Sounding (MARSIS) instrument onboard the Mars Express orbiter obtained the first subsurface profiles from Planum Boreum, which showed a strong radar return from the base of the deposits (Picardi et al., 2005; Phillips et al., 2008, SOM; Selvans et al., 2009). More recently, observations from the Shallow Radar (SHARAD) instrument onboard the Mars Reconnaissance Orbiter (MRO) show a weaker, diffuse radar return from the base, but many more internal reflections from overlying layered materials (Phillips et al., 2008). Taken together, these results exemplify the complementary nature of the two instruments, with MARSIS providing greater depth of penetration and SHARAD finer vertical resolution (~10 m in water ice, vs. ~100 m for MARSIS) (Seu et al., 2007b). The work presented here will focus on the SHARAD observations, which provide greater detail of internal structures and thus allow a more direct comparison to image-based geologic interpretations.

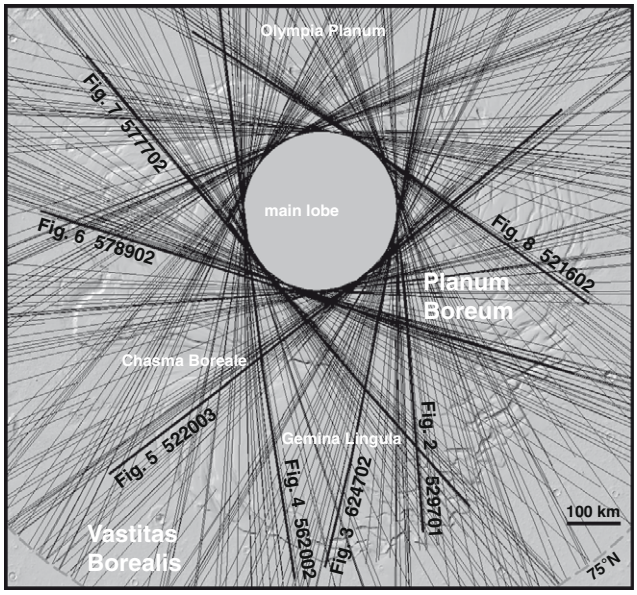

Fig. 1. Polar stereographic location map of Mars' north polar region, showing SHARAD ground tracks (tangent to limit of MRO orbit at ~87.4°N) for observations used in this study, overlain on MOLA shaded relief. Bold lines are labeled with observation numbers corresponding to radargrams shown in Figs. 2–8. Zero longitude is at bottom-center of figure.

In the following section, we describe the SHARAD observations and the methods we use for analyzing them. In Section 3, we discuss our rationale for assigning and interpreting radar units and their boundaries, highlighting features of Planum Boreum revealed by the radar (Figs. 2–8). In Section 4, we explain our methods for interpolation, extrapolation, and conversion to depth of the unit boundaries, which were interpreted originally in delay time. These steps yield isopach and elevation maps (Figs. 9 and 10) as well as precise volume estimates for the NPLD as a whole and for its constituent radar units (Table 1). In Section 5, we present a discussion of our results and their implications for the history of the NPLD and the Martian climate. We also briefly discuss smaller-scale features, such as unconformities and structures associated with troughs. In Section 6, we summarize our most important findings and outline avenues for future research.

2. Observations

The SHARAD instrument is a chirped-pulse sounding radar with a 10-MHz bandwidth centered at 20 MHz, which yields a free-space range resolution of 15 m (8.4 m in water ice with a real permittivity of 3.15). The altitude of the MRO orbit varies between about 250 and 320 km, allowing a lateral resolution at the surface of ~3–6 km (1–2 Fresnel zones), which can be reduced in the azimuth (along-track) direction to 0.3–1.0 km with synthetic-aperture focusing. See Seu et al. (2007b) for a detailed discussion of the SHARAD experiment.

A SHARAD observational campaign for the north polar region has yielded dense coverage in this region, with observations acquired on more than 1300 orbits through March 2009. Typically, SHARAD observations of the polar region are taken over a 700-s period and span 20° of latitude on either side of the pole (~2000 km), but the duration and coverage of individual data takes may vary substantially. We selected 358 observations for this study, providing the coverage shown in Fig. 1. We present portions of six representative observations where they extend across Planum Boreum in Figs. 2–8.

Subsurface radar data are typically displayed as radargrams, with distance along track shown horizontally and power vs. delay time displayed vertically in an image format (e.g., Figs. 2–8, top panel). While delay time is roughly analogous to depth, such radargrams exhibit a geometric distortion due to the combination of surface topography and the difference in signal speed in free space vs. that in typical geological materials (e.g., regolith or water ice). Furthermore, reflections from off-nadir surface features may arrive at delay times similar to those from true subsurface interfaces, and a careful analysis of the sources of such surface clutter is required. We now consider approaches to accounting for these effects.

To address the geometric distortion, one may convert the delay-time radargram to depth on a sample-by-sample basis as:

$$\Delta d_i = c\Delta t/2\varepsilon_i^{1/2} \quad (1)$$

where Δd_i is the depth interval for the ith sample in delay time, c is the speed of light in free space, Δt is the delay-time sampling interval, and ε_i is the real permittivity of the traversed medium, with the divisor of two accounting for two-way travel (i.e., radar transmit and receive paths). To create depth-converted radargrams, we first identify the samples associated with the surface return and then apply Eq. (1), assuming values for ε_i of 1.0 above the surface and 3.15 below, where the latter value is typical of pure water ice under Martian surface conditions (Johari, 1976; Mätzler and Wegmüller, 1987; Grima et al., 2009). Where the initial surface return is off-nadir, a distortion in the depth-converted radargram can occur (e.g., see Figs. 3 and 8). Our assumption of nearly pure water ice in the NPLD is based on estimates of their lithic content derived from

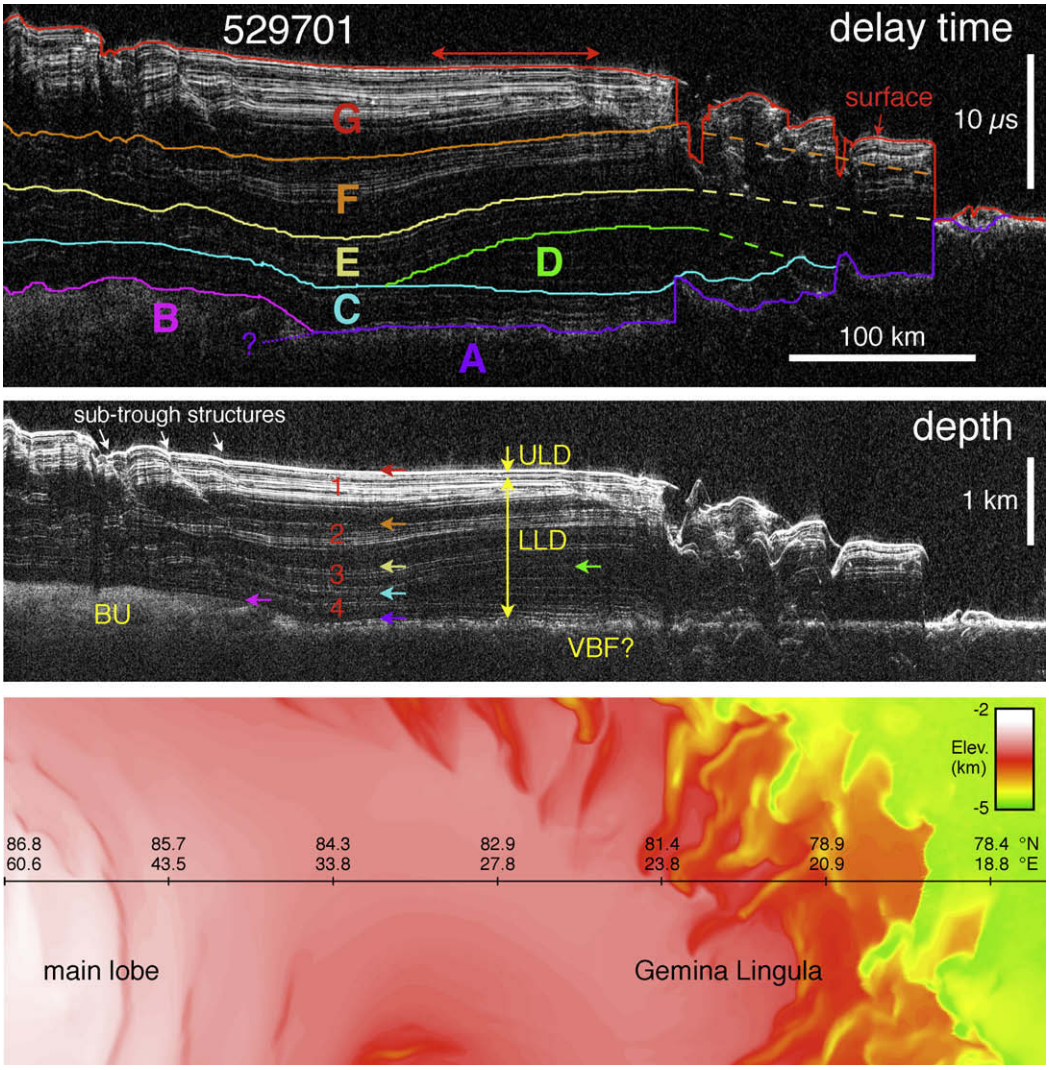

Fig. 2. SHARAD observation 529701, crossing the topographic saddle between the main lobe and Gemina Lingula. Delay-time radargram (top panel) is overlain with interpreted boundaries for radar units A–G, dashed where extrapolated. Extrapolated boundaries may not align with radar reflectors (see text). Unit A extends beneath Unit B, but the contact is not typically evident in SHARAD data. Red arrow shows lateral extent of apparent angular unconformity at ~2.5 μs delay time in Unit G. Depth-converted radargram (middle panel), which is created by assuming a subsurface real permittivity of 3.15 (nearly pure ice), shows proper geometric relationships at ~45:1 vertical exaggeration, with packets of Phillips et al. (2008) in red and approximate correlations to geological units of Tanaka (2005) in yellow (VBF: Vastitas Borealis Formation; BU: basal unit; LLD: lower layered deposits; ULD: upper layered deposits). Colored arrows show reflectors corresponding to unit boundaries in upper panel. Layer discontinuities occur progressively closer to the southern extent of the BU with depth (white arrows). MOLA elevation map (bottom panel) shows location of ground track.

the attenuation of radar signals (Phillips et al., 2008; Picardi et al., 2005; Grima et al., 2009).

The potential for surface clutter may be addressed qualitatively by examining a map of surface topography in the vicinity of the radar ground track (e.g., Figs. 2–8, third panel). Radar signals reflected from spacecraft-facing facets of topographic highs or depressions on either side of the ground track may produce a return that is delayed in time relative to the nadir surface return in proportion to the difference in distance from the spacecraft. Examples of strong surface clutter are identified in Fig. 6, where returns from surface troughs offset from the ground track appear as dipping reflectors subsequent to the surface returns. For subtle features, a more quantitative approach to characterizing clutter may be taken by producing simulated radargrams, which can be generated from topographic information such as an elevation map of Mars Orbiter Laser Altimeter (MOLA) data. Such synthetic radargrams are used routinely in distinguishing probable subsurface detections from surface clutter in terrestrial studies (e.g., Holt et al., 2006) and in MARSIS and SHARAD data (e.g., Picardi et al., 2005; Holt et al., 2008; Plaut et al., 2009). Extra caution is advised when interpreting radar observations made in the vicinity of areas with sparse elevation data, such as the regions poleward of 87° latitude, as surface features missing from the elevation maps may yield clutter in the radar data that does not appear in the simulated radargrams. We point out an example in Fig. 7, where troughs poleward of 87°N that are seen in the Viking image mosaic (fourth panel) are missing from the MOLA map (third panel), and these troughs produce surface clutter visible in the radargram (first panel) but not in the MOLA-generated simulation (bottom panel).

3. Radar unit delineation

In Planum Boreum, SHARAD radargrams show a packet of closely spaced, strong reflections to ~5 μs delay time below the surface. These reflections are typically conformal with the surface return, but occasionally include apparent angular unconformities at depth (e.g., see Fig. 2). The packet of strong reflectors is generally

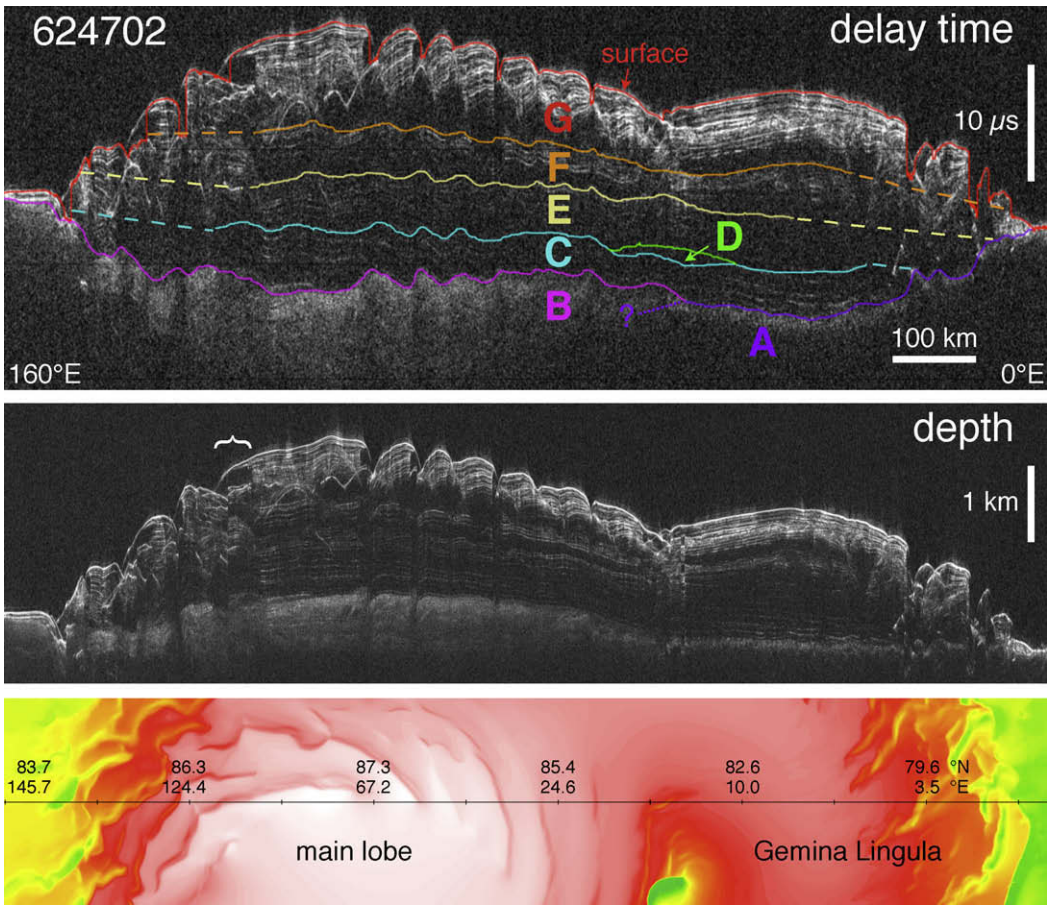

Fig. 3. Radargrams for SHARAD observation 624702 in delay time (top panel) and depth (middle panel; vertical exaggeration ~100:1), extending from Olympia Planum, across the main lobe, just east of the head of Chasma Boreale, and across Gemina Lingula. MOLA elevation map (bottom panel) shows location of ground track. Brace in depth radargram shows zone of distortion due to off-nadir surface returns. Radar units, depth-conversion methods, and MOLA scale same as in Fig. 2.

underlain by a zone of much weaker or negligible returns ~2–3 μs in round-trip delay time. At later delay times, several similar sequences of packet–inter-packet reflections follow, but the reflectors are typically reduced in number, frequency, and relative backscattered power. Much of this behavior may be attributable to attenuation of the radar signal by transmission and path losses rather than actual increases in layer thickness or reductions in dielectric contrast (e.g., see Nunes and Phillips, 2006). The individual reflectors within packets and the repeated packet sequences represent two periodicities, which Phillips et al. (2008) related to global climatological cycles of Mars driven by orbital and rotational dynamics (Laskar et al., 2002). In designating the units within the zone of packet sequences for this study, we chose the top of each packet as the unit boundary, with the inter-packet zone included in the base of the same unit. We found that the uppermost reflections in the packets are relatively consistent and traceable across many radargrams, whereas the lowermost reflections in the packets occur intermittently, implying a less distinct transition. Beneath these packet–inter-packet sequences, SHARAD radargrams typically show zones of reflections that are diffuse (but significantly above the instrument noise background) with durations of 5–10 μs beneath most of the main lobe and 1–3 μs beneath Gemina Lingula, portions of the main lobe in the eastern hemisphere, and the topographic saddle between the two lobes. The duration of the latter zone of diffuse energy is similar to that observed just below the surface of the Vastitas Borealis materials that surround Planum Boreum.

We designated a working set of radar-based geologic units (Fig. 2), beginning with Unit A as the thinner diffusely reflective zone, which we interpret as a likely extension of the Vastitas Borealis Interior Unit (ABvi) (Tanaka et al., 2008)—often referred to as the Vastitas Borealis Formation (VBF) (Tanaka and Scott, 1987)—beneath Gemina Lingula. Unit B, the thicker diffusely reflective zone, has been correlated with the BU discussed earlier (Phillips et al., 2008). Although not evident in most of the SHARAD data shown here, Unit A extends beneath Unit B and sometimes displays a weak reflection under the main lobe; this same contact yields the strong basal reflections seen by MARSIS (Picardi et al., 2005; Phillips et al., 2008, SOM; Selvans et al., 2009). Hints of a return from this depth are seen in SHARAD observation 522003 (Fig. 5). Additionally, a reflector likely corresponding to Unit B appears only rarely in radargrams over Olympia Undae (not shown here). Given these inconsistent returns, we did not attempt to map Units A and B in these areas, nor do we map them where they occur at the surface beyond Planum Boreum. Overlying Units A and B is a set of quasi-parallel reflecting horizons ~200–300-m thick that appear to extend throughout the NPLD, which we designate as Unit C. The upper boundary of this unit is identified by the presence of a 'wedge' of nearly parallel, reflecting interfaces up to ~300-m thick that is confined to the eastern part of Gemina Lingula and defined here as Unit D (Figs. 2, 3 and 7). Another set of near-parallel reflectors, often associated with an inter-packet zone of modestly diffuse returns at its base, appears to be 'draped' over those of Units C and D, and we designate these as Unit E. This unit is in turn overlain by a packet–inter-packet sequence identified here as Unit F. Finally, Unit F is itself overlain by the uppermost packet–inter-packet sequence that extends to the surface and is designated as Unit G.

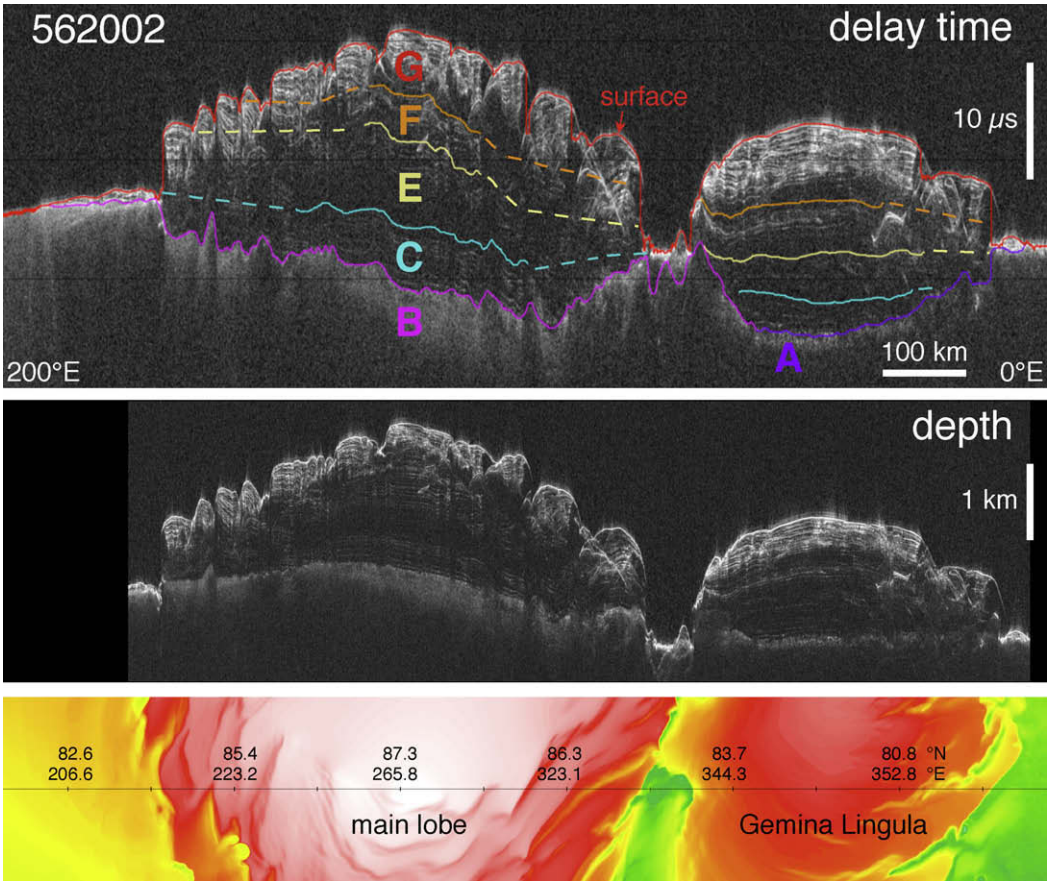

Fig. 4. Radargrams for SHARAD observation 562002 in delay time (top panel) and depth (middle panel; vertical exaggeration ~100:1), extending from Olympia Planum across the main lobe, Chasma Boreale, and Gemina Lingula. MOLA elevation map (bottom panel) shows location of ground track. Radar units, depth-conversion methods, and MOLA scale same as in Fig. 2.

Using commercial seismic-data analysis software (provided by SeisWare International Inc.), we delineated the unit contacts, beginning with radargrams that cross the topographic saddle between the main lobe and Gemina Lingula. The radar units described above are best resolved in this area, which is topographically smooth over hundreds of kilometers, having no troughs and few surface undulations (Rodriguez et al., 2009), and thus we chose to begin correlations of unit boundaries here. Processing of the SHARAD data employs a delay-time datum that varies from one radargram to another. Unit correlation and datum adjustment are handled within the data analysis software, which allows the display on each radargram of interpreted horizons from other, intersecting radargrams, and the interactive adjustment of the radargram datums. Designated unit boundaries were transferred in this fashion from one radargram to another, with datums adjusted accordingly, and the units were systematically extended as far as possible throughout Planum Boreum (see solid colored lines in the top panels of Figs. 2–8).

As demonstrated by the depth-converted versions of the radargrams (second panels of Figs. 2–8), many of the reflector undulations seen in the delay-time radargrams are actually due to the combination of complex topographic relief at the surface and the difference in radar wave speeds of the atmosphere and subsurface materials. The true geometry of the subsurface returns is shown to be much smoother in the depth-converted radargrams—for example, those returns corresponding to the top of Unit A are nearly flat-lying everywhere and those associated with the top of Unit B appear as a smoothly varying dome, with one notable exception. From right to left across the depth-converted radargram for SHARAD observation 577702 (second panel in Fig. 7), one sees the top of Unit B rising gradually before a 'precipitous' drop of ~600 m near 85°N, 260°E. While the elevation change appears quite abrupt on the vertically exaggerated depth radargram, the actual slope is only ~3–4° (see discussion in Section 5). Continuing on, the boundary again takes on a dome-like profile as it approaches the periphery of Planum Boreum near eastern Olympia Planum. In addition, the character of the radar returns changes in this zone such that the backscattered power at the boundary is greater and the diffuse power normally associated with the underlying Unit B is diminished. The radargram for SHARAD observation 578902 demonstrates similar behavior across this region, including topographic and reflectivity anomalies in Unit B (see Fig. 6), and MARSIS data show disruptions in this same region (Selvans et al., 2009).

4. Mapping

Once the unit boundaries were delineated on the selected delay-time radargrams, we used the data analysis software to map them to a regular grid with cells of 2.7 km × 2.7 km. First, we interpolated the surface horizon, mapping it everywhere poleward of 75°N. Next, we interpolated the tops of the basal Units A and B, which together completely cover the region at the base of the NPLD out to their intersections with the surface grid. Then, as we interpolated the internal boundaries (tops of Units C–F), we also extrapolated them to the periphery of the NPLD to their intersections with either the surface grid or the basal grid. We differenced the

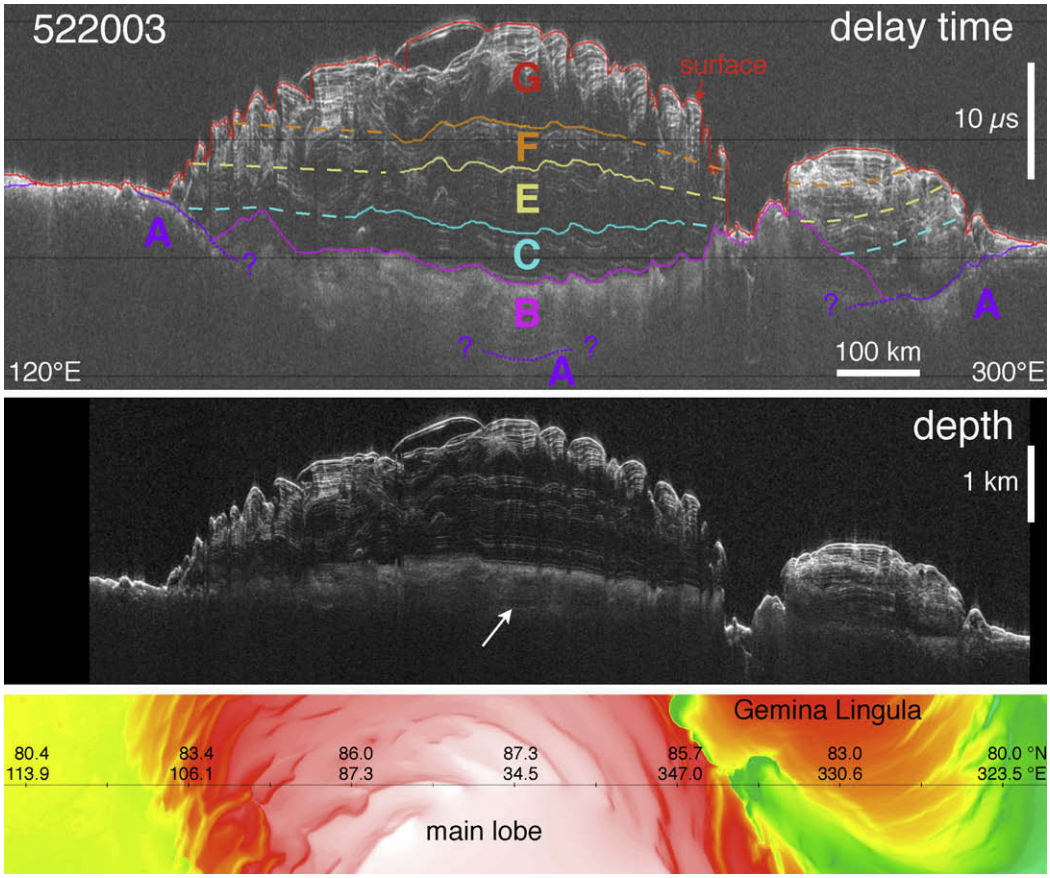

Fig. 5. Radargrams for SHARAD observation 522003 in delay time (top panel) and depth (middle panel; vertical exaggeration ~100:1), extending from Olympia Mensae across the main lobe, Chasma Boreale, and Gemina Lingula. MOLA elevation map (bottom panel) shows location of ground track. Arrow indicates rarely seen returns from below Unit B that are interpreted as possible Top Unit A. Radar units, depth-conversion methods, and MOLA scale same as in Fig. 2.

radar-unit delay-time grids, converting them to thickness using Eq. (1) and assuming a subsurface real permittivity of 3.15 to produce the isopach maps shown in Fig. 9. From these maps, we computed the average thickness, extent by area, total volume, and percentage of volume in the extrapolated region for each of the radar units and for the NPLD as a whole, and we report these values in Table 1. Additionally, we counted the typical number of radar layers within each unit and we report estimates for their average thicknesses, also in Table 1. The total NPLD volume of 821,000 km^3, which represents a global-equivalent layer of 5.7 m, is 27% smaller than the estimate by Smith et al. (2001) of 1,140,000 km^3 (where they assumed no flexure and pure water ice). While they used a slightly larger area (1,120,000 km^2 vs. our 949,000 km^2), most of the 319,000-km^3 difference in volume is due to our exclusion of the BU from these calculations. An effort to better constrain the volume of the BU from MARSIS observations is ongoing (Selvans et al., 2009).

We created an elevation map for the base of the NPLD together with the surrounding surface (Base NPLD map in Fig. 10) by first converting the surface delay-time grid to elevation (Surface map in Fig. 10) and then subtracting the NPLD isopach map from it. By progressively adding each of the isopach maps for Units C–F to the Base NPLD elevation map, we obtained the set of elevation maps for these internal unit boundaries shown in the other panels of Fig. 10. In each map shown in Figs. 9 and 10, the region poleward of the oval near 87.4°N has no coverage by SHARAD and hence the values there are entirely interpolated. This region is included in the area and volume estimates shown in Table 1 and represents about 13% of the volume for each radar unit and for the NPLD as a whole.

The NPLD isopach map, which represents all of the material overlying Units A and B (i.e., Units C–G collectively), demonstrates that much of the difference in elevation between Gemina Lingula and the main lobe (see Surface elevation map in Fig. 10) can be attributed to the BU deposits (Unit B), with the stack of NPLD layers in Gemina Lingula approaching the same maximum thickness of ~2 km that it does in the main lobe. At their highest point, the BU deposits stand about 1 km above the surrounding terrain (see Base NPLD map in Fig. 10), which presumably represents their maximum thickness above the flat-lying Vastitas Borealis deposits.

The isopach maps for Units C, E, and F show that these three units are of similar thickness and geographic distribution to each other, each relatively uniform in thickness in the interior of Planum Boreum and tapering quickly at the periphery. This similarity suggests that the deposition of these units was a repetitious process that did not vary greatly in its intensity. In contrast, Unit D appears wedge-shaped in its thickness variations and is geographically restricted to a substantially smaller area in eastern Gemina Lingula. Relative to Units C, E, and F, the uppermost sequence—Unit G—is thicker, has a more dome-like profile, and is restricted to a somewhat smaller region, tapering out further up in Planum Boreum. An important caveat is that the distal geographic extent of the internal unit boundaries is controlled to a large extent by our rather simplistic extrapolation of the boundaries out to the periphery of the deposits. It is a distinct possibility that these extrapolations do a poor job of tracking actual depositional or erosional boundaries—for instance, one might argue that the highly reflective zones near the periphery actually correspond largely to Unit G rather than to Units E, F, and C (e.g., see Fig. 5 near 84°N,

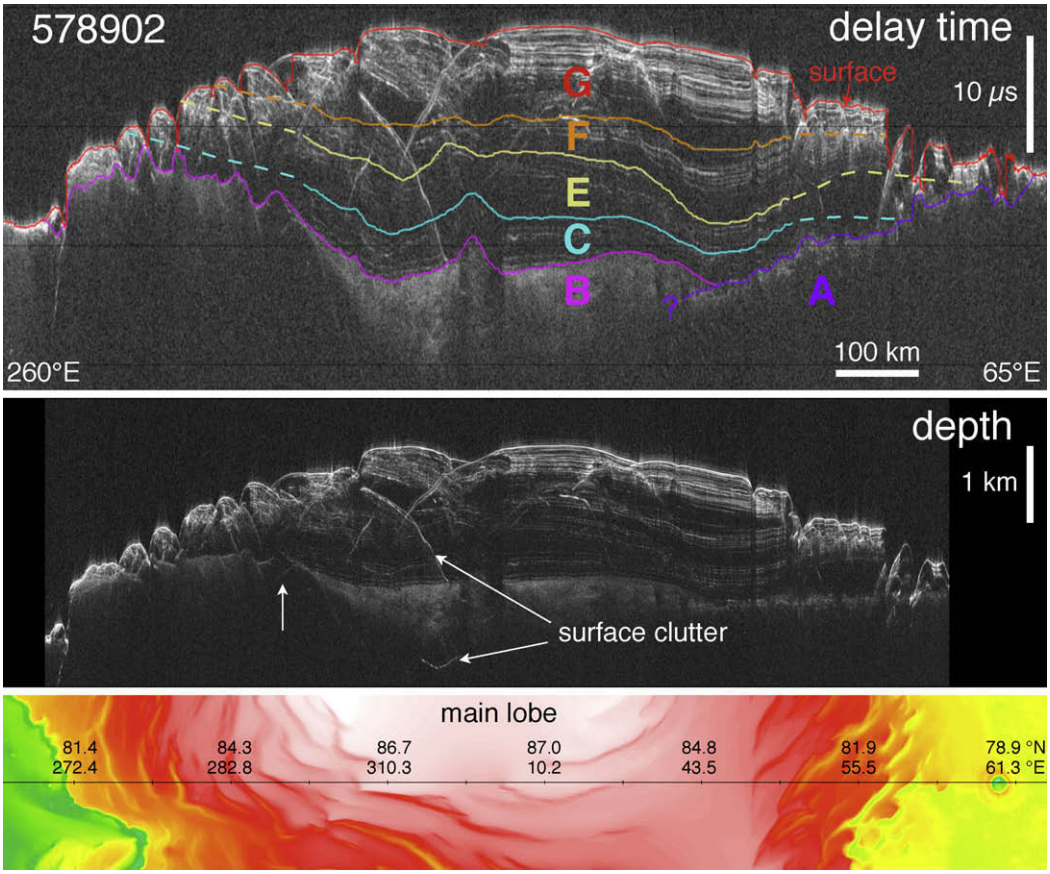

Fig. 6. Radargrams for SHARAD observation 578902 in delay time (top panel) and depth (middle panel; vertical exaggeration ~100:1), extending from Rupes Tenuis across the main lobe to ~62°E. MOLA elevation map (bottom panel) shows location of ground track. Pronounced surface clutter comes from trough walls running subparallel to ground track. Vertical arrow shows location of anomalous topography and reduced internal reflectivity of Unit B (see discussion in text). Radar units, depth-conversion methods, and MOLA scale same as in Fig. 2.

100°E and Fig. 6 near 84°N, 280°E). In that case, the distal extent of the interior units is likely to be substantially different than portrayed in the isopach maps (Fig. 9), wherein the extent of Unit G ought to be greater and that of Units E, F, and C ought to be lesser. Nevertheless, the accuracy of the maps is high in their interiors where we explicitly chose the boundaries, and we believe that they are broadly representative of the actual thicknesses and volumes of the materials associated with these units. In any case, the estimates of thickness, extent, and volume for the NPLD as a whole are robust.

5. Discussion

For a particular target medium, a reflecting horizon in SHARAD data includes the radar returns from all dielectric interfaces within the vertical-resolution cell (~8.4 m in pure water ice). The strong, parallel reflections that characterize the packet regions are only somewhat weaker than the radar echoes from the surface. For example, the echo power of the brightest subsurface reflector below the saddle region in observation 529701 (Fig. 2), occurring at about ~190-m depth, is only ~2 dB down from that of the surface return. Other intermediately bright reflections in this zone, which are more typical of Unit G throughout Planum Boreum, are ~6 dB down from the surface return. The reflectivity of the surface echo is ~0.08, so that of the brightest subsurface return is at least 0.05 (ignoring attenuation), which requires a real permittivity of 7.7 in contrast with the assumed value of 3.15 for clean ice. Such a high permittivity suggests a minimum dust loading of ~85%, approaching 100% if reasonable values of attenuation in the ice are included. Many of the other, fainter reflections in this region could be explained by a thin layer with ~30% dust content.

The fact that the strong echoes exhibit relatively modest power reduction with increasing depth indicates that the total column loss due to attenuation by lithic materials (dust or sand) is very low—modeling suggests at most a few percent of the total NPLD volume (Picardi et al., 2005; Nunes and Phillips, 2006). Thus, each of the intermediate-power reflections (those ~6 dB down from the surface return) might arise from one of two mechanisms: (1) a single layer with a high concentration of dust or sand no more than ~1 m in thickness (based on a ~2-km layer with 40–50 bright reflectors and a 1–2% column abundance of lithic material); or (2) alternating, parallel bands of clean and moderately lithic-rich ice within the vertical-resolution cell. In the latter case, it is the net reflectivity of these densely spaced layers that creates the observed bright return. For example, if the echo power is an incoherent sum of reflections, then about four 1-m layers with ~30% dust in ice could produce echos with a ~6-dB reduction in power relative to the surface.

Given that image data clearly show pervasive layering at scales well below the SHARAD vertical-resolution cell size, we favor the multi-layer model as representative of at least the intermediate reflections from the banded packets. However, SHARAD data alone cannot resolve the nature of any given bright reflector. The multi-layer model may introduce complications with regard to interference between returns from interfaces separated by fractions of

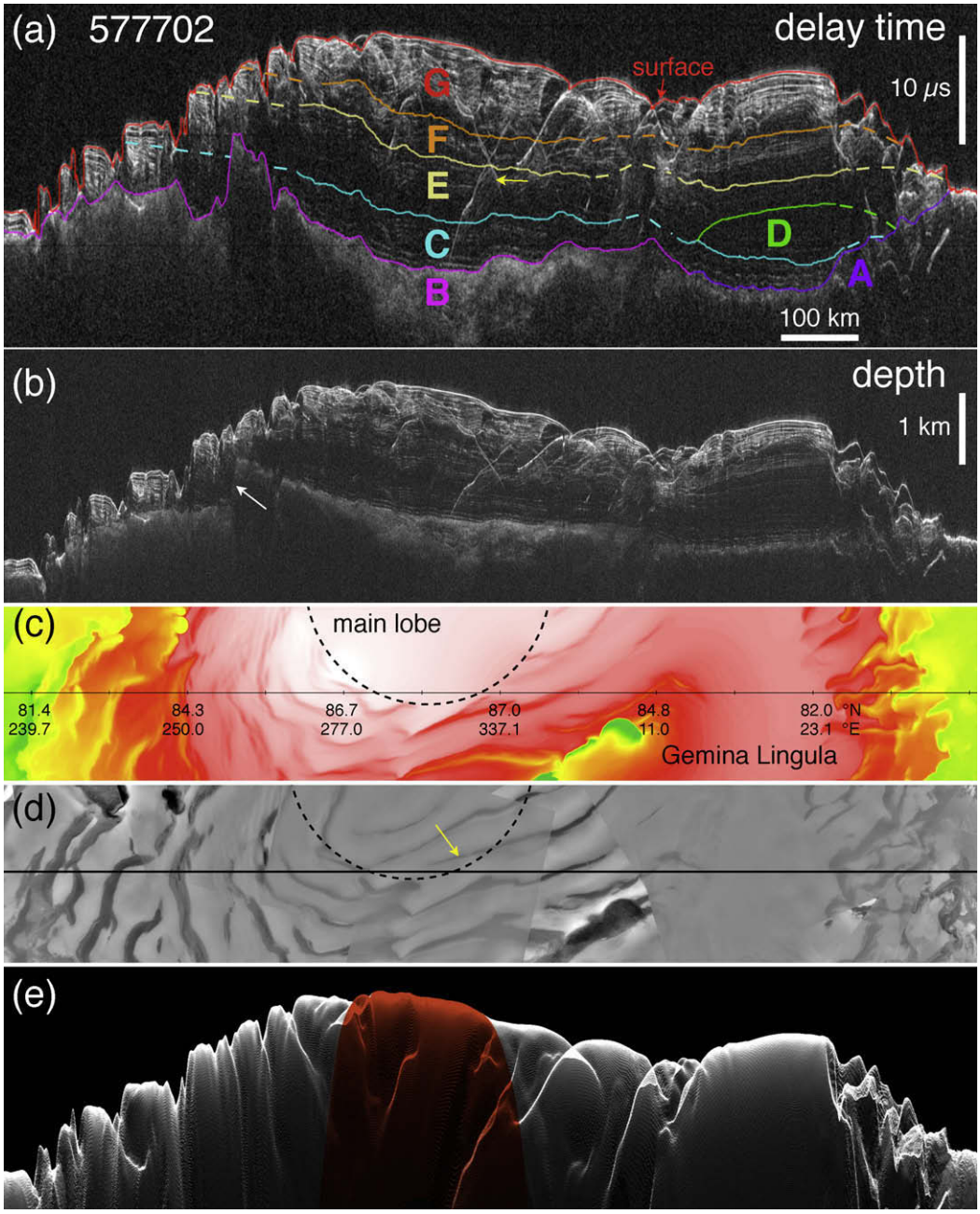

Fig. 7. Radargrams for SHARAD observation 577702 in (a) delay time and (b) depth (vertical exaggeration ~100:1) extend from Olympia Planum across the main lobe and Gemina Lingula. (c) MOLA gridded elevation map and (d) Viking MDIM mosaic show location of ground track. (e) Simulated delay-time radargram from MOLA data and a geometrical optics, facet-based scattering model with incoherent summation (Holt et al., 2006) identifies as surface clutter many returns with steep apparent dip. Other returns (e.g., yellow arrow in (a)) do not appear in the simulation but are attributable to troughs (e.g., yellow arrow in (d)) poleward of the ~87°N limit of the MOLA data (dashed black semicircles). Red shading in (e) shows region affected by the no-data zone. White arrow in (b) identifies a large elevation anomaly at top of Unit B. Radar units, depth-conversion methods, and MOLA scale same as in Fig. 2.

the wavelength in the medium. While we cannot determine the dielectric structure of the NPLD at scales below the SHARAD vertical resolution, it is plausible that bright echos arise from alternating, closely spaced layers of clean ice and layers of modest dust abundance.

Radargrams that cross Chasma Boreale (Figs. 4 and 5) clearly show that Unit B (i.e., the BU) extends southward into the Gemina Lingula lobe. These radar results confirm an earlier suggestion by Tanaka et al. (2008) based on surface images that the BU is not entirely confined to the main lobe as was originally thought (Byrne and Murray, 2002; Fishbaugh and Head, 2005). In discussing scenarios of Chasma Boreale formation, Fishbaugh and Head (2005) suggested that its location may have been influenced by the southern boundary of the BU, but its extension into Gemina Lingula revealed by the radar data indicates that the relationship between the BU and Chasma Boreale is not so straightforward. The possibility remains that pre-existing topographic features adjacent to and/or atop the BU played a pivotal role in the formation of the Chasma (Holt and Safaeinili, 2009).

In the earlier image-based analyses of the BU, it was thought that these deposits extended nearly everywhere beneath the main lobe, but the SHARAD data show that the BU is absent below a large portion of the main lobe to the east of the saddle region (~20°E–110°E) and south of ~85°N (compare the boundary be-

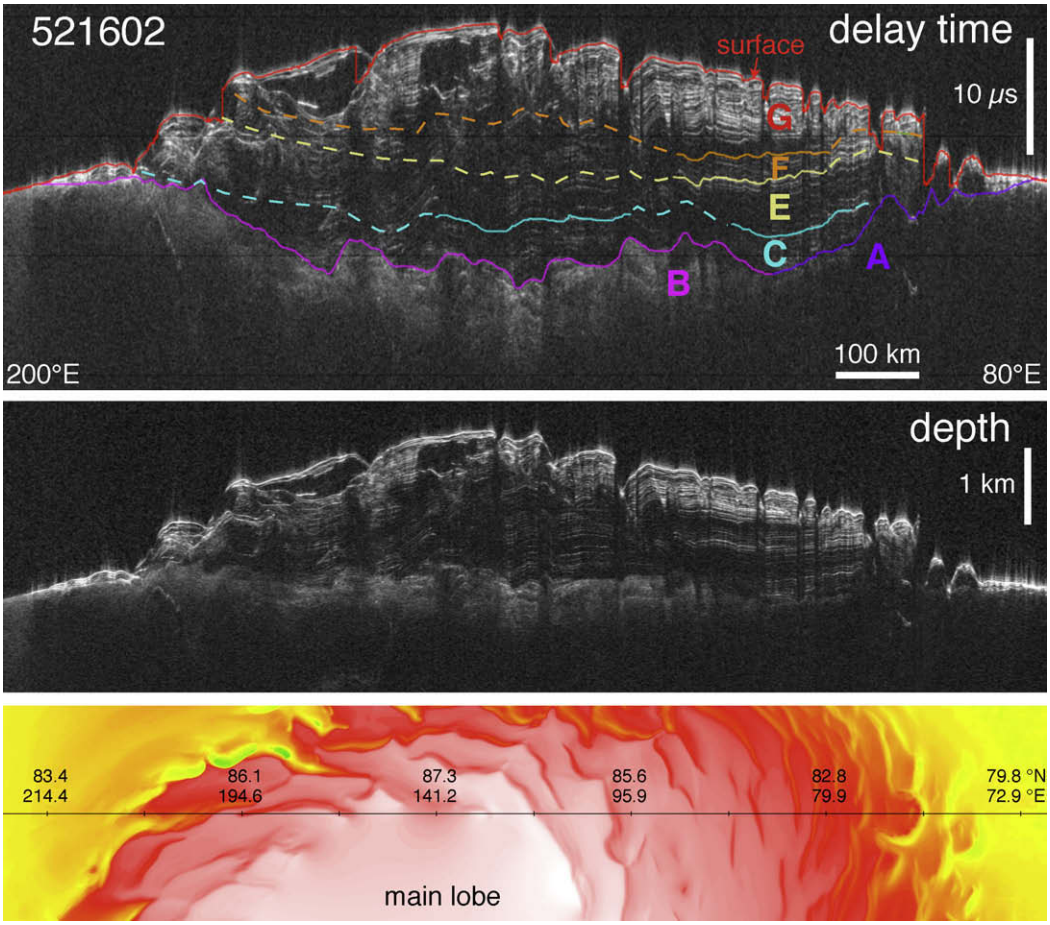

Fig. 8. Radargrams for SHARAD observation 521602 in delay time (top panel) and depth (middle panel; vertical exaggeration ~100:1), extending from Olympia Planum across the main lobe to ~72°E. MOLA elevation map (bottom panel) shows location of ground track. Radar returns are highly disrupted and interpreted unit boundaries are mostly extrapolated in this region that borders Olympia Planum. The morphology of the basal unit is inaccurate in the depth-converted radargram due to off-nadir surface returns. Radar units, depth-conversion methods, and MOLA scale same as in Fig. 2.

tween Units A and B with the BU boundary of Fishbaugh and Head, 2005, on the surface elevation map in Fig. 10). SHARAD radargrams clearly and consistently show the absence of Unit B in this region of the main lobe (e.g., Figs. 5, 6 and 8). Either the BU was never deposited in this region or it was eroded away prior to the deposition of Unit C.

The elevation anomaly in Unit B that we mention in Section 3 and identify in SHARAD observations 578902 (Fig. 6) and 577702 (Fig. 7) provides an intriguing puzzle. The fact that this same feature occurs at similar delay times on all radargrams crossing this region and the lack of surface features that might cause clutter at these delay times or induce large errors in the depth conversion provides confidence that the returns are indeed attributable to a subsurface elevation anomaly atop Unit B. In map view (see Base NPLD map in Fig. 10), this feature appears as a longitudinally elongated peak at the highest elevation of Unit B, with relatively steep slopes to the south and shallower slopes to the west, north, and east. While it is tempting to suggest a normal fault in the BU that was subsequently buried by the NPLD as an explanation, when one accounts for the vertical exaggeration of ~100:1 in the depth radargrams, the true slope of the putative fault plane is actually quite low (~3–5°), and normal faults of such low angle are rare. Perhaps a more likely explanation is that this portion of Unit B represents a remnant of an earlier polar ice deposit, and the ~600-m-high slope is analogous to scarps of present-day Planum Boreum. For example, Fig. 7 shows an interior surface scarp of similar height and slope angle about 80 km south (left) of the anomalous feature (identified by the white arrow). Such a remnant deposit may contain less internal contamination by lithic materials than elsewhere in Unit B and perhaps a thick lag deposit on its surface, which could explain the reduced power in diffuse radar returns from within the unit and increased power of the radar return from the top of the unit (e.g., see Figs. 6 and 7). Another possibility is that the anomalous feature is an erosional remnant of a pedestal preserved by the ejecta of a large impact into Unit B that was subsequently buried by deposition of the overlying units. An analogous feature might be the irregular, 700-m-high plateau around Escorial crater that is currently exposed at the surface and thought to be made up of Rupes Tenuis materials (Tanaka et al., 2008).

With the exception of Unit D, all of the NPLD radar units extend across much of the main lobe and Gemina Lingula, indicating that deposition occurred regionally throughout most of the NPLD formation history. The series of elevation maps in Fig. 10 suggests that the highest point (or at least the highest point south of the unobserved area poleward of 87°N) remained near 85°N, 260°E for a long period of time, presumably established during an erosional event represented by the base of the NPLD and persisting through the deposition of Units C–F. While there is some evidence for internal unconformities that may represent erosional periods (e.g., within Unit G in Fig. 2), the units and their internal layers are remarkably conformable to each other in most areas. Any erosion that may have occurred must have either stripped materials off uniformly or been restricted geographically, perhaps largely confined to the periphery of Planum Boreum.

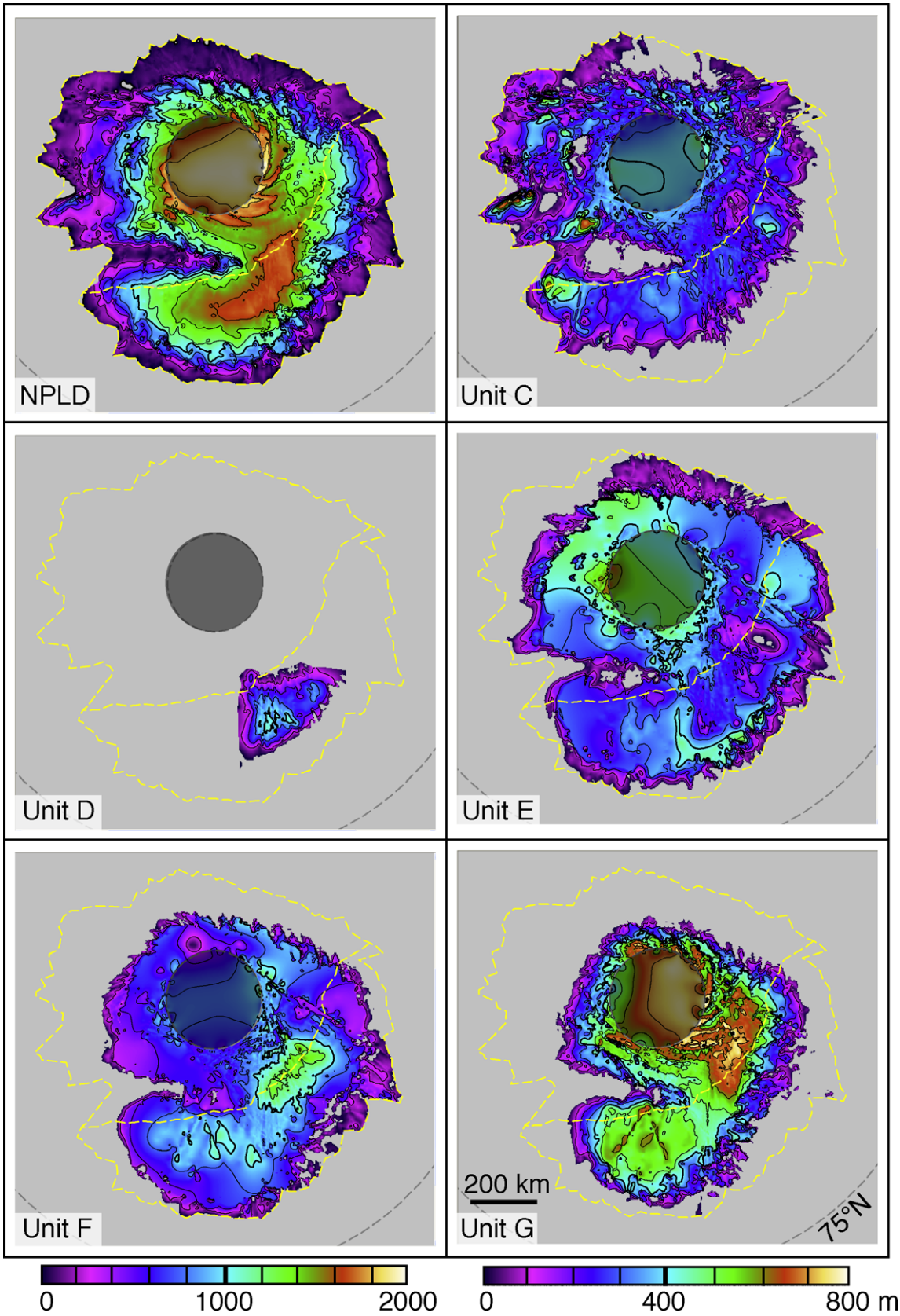

Fig. 9. Polar stereographic isopach (thickness) maps for the entire NPLD and for Units C–G from SHARAD data, assuming subsurface real permittivity of 3.15 (nearly pure water ice). Contour intervals are 200 m for NPLD map (left scale bar) and 100 m for individual unit maps (right scale bar). On each map, a dashed yellow outline encompasses basal Units A (lower right section) and B (upper left section). Shaded oval extends to northernmost extent of MRO ground tracks at ~87.4°N.

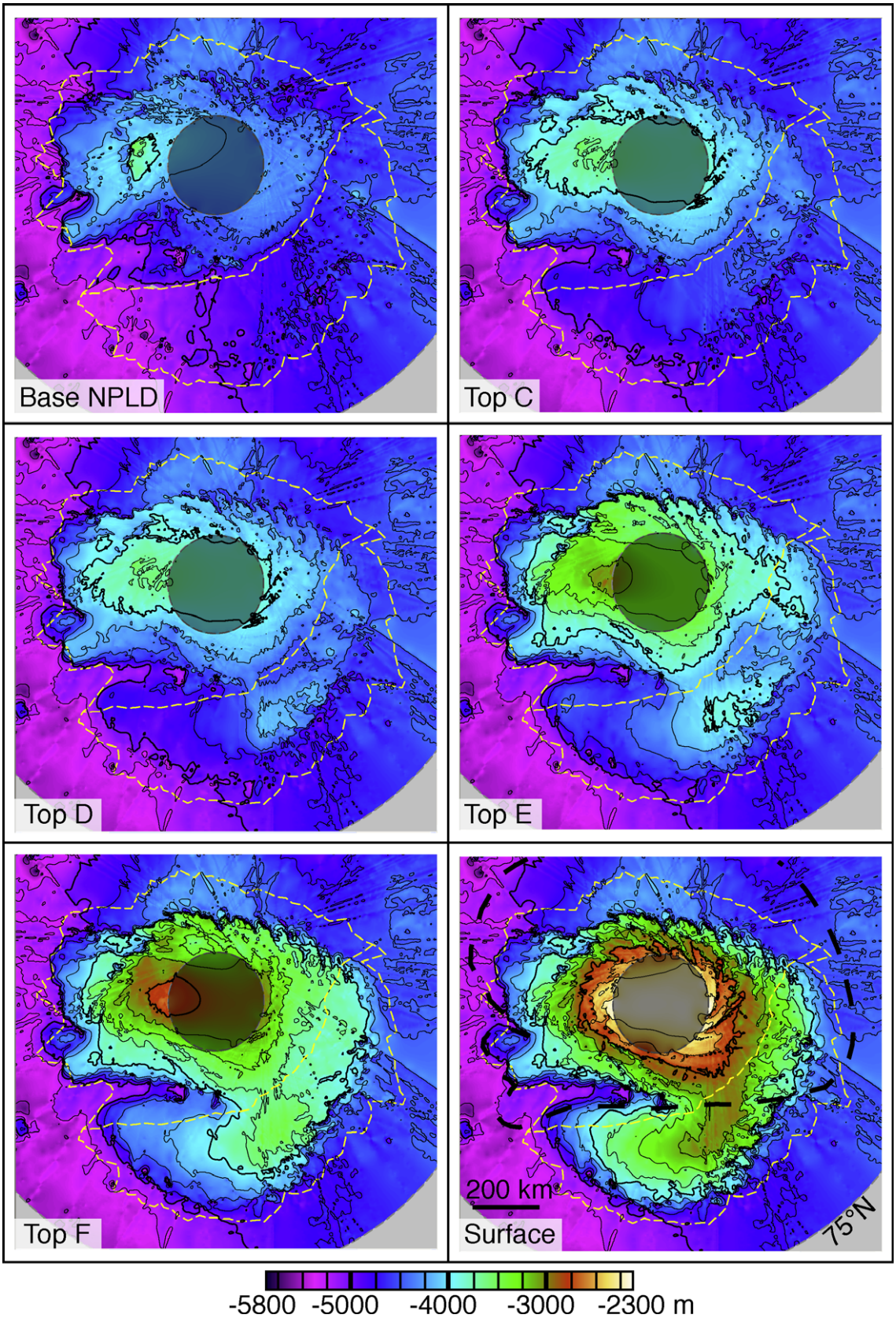

Fig. 10. Polar stereographic elevation maps of the base of NPLD (i.e., top of Units A and B), the top of Units C–F, and the surface, derived from SHARAD data. A subsurface real permittivity of 3.15 (nearly pure water ice) is assumed. Contour interval is 250 m. On each map, a dashed yellow outline encompasses basal Units A (lower right section) and B (upper left section). Shaded oval extends to northernmost extent of MRO ground tracks at ~87.4°N. Black dashed line in surface map (lower right panel) is limit of basal unit as mapped by Fishbaugh and Head (2005).

Table 1
NPLD radar-unit number of layers, thicknesses, areas, and volumes.

Unit	# Layers	Mean unit thickness (m)	Mean layer thickness (m)	Area (km^2)	Volume (km^3)	Extrapolated volume (%)
G	21	432	21	537,000	232,000	19
F	12	254	21	672,000	171,000	34
E	10	281	28	815,000	229,000	45
D	4	192	48	71,000	14,000	29
C	6	227	38	765,000	174,000	44
NPLD	48[a]	864	18	949,000	821,000	35[b]

[a] Does not include layers in the geographically isolated Unit D.
[b] Average for internal units; total NPLD volume uses surface and basal picks with no extrapolation.

Unit D represents a potentially important exception to the above generalizations. It is likely that these deposits have been greatly eroded on the periphery together with the overlying units (Holt and Safaeinili, 2009), and it is possible that detailed mapping of sub-unit layering may reveal a greater lateral extent for Unit D. In either case, it is evident from our mapping that Unit D is more variable in thickness and restricted in extent than the overlying units and thus represents substantially different depositional and/or erosional patterns early in the history of the NPLD.

Estimates for the age of the NPLD based on correlations of layering seen in image data with Mars' orbital characteristics or with other data range from a few million years to hundreds of millions of years (Laskar et al., 2002; Milkovich and Head, 2005; Tanaka et al., 2008). The lower estimates are generally based on climate modeling studies (Laskar et al., 2002; Milkovich and Head, 2005; Levrard et al., 2007), whereas the higher estimates are constrained by sparse but relatively large craters that may represent impacts in some of the lower sequences of the NPLD and by an unconformity in the upper part of the NPLD (Tanaka, 2005; Tanaka et al., 2008, 2009).

Modeling of polar-ice accumulation that incorporates the evolution of orbital characteristics together with effects from the periodic formation of lag deposits was performed by Levrard et al. (2007), who obtained a maximum age of 4.2 Ma for the NPLD (see base graphs in Fig. 11). Their results suggest that periods when the amplitude of insolation variation is low, which correspond to periods of lower-amplitude obliquity variations (cf. second panel in Fig. 12, taken from Fig. 2d of Laskar et al., 2002), have relatively rapid accumulation of ice in the polar region. The intervening times, when insolation varies more widely, are predicted to yield alternating periods of accumulation and sublimation that cause the concentration of lithic materials in lag deposits (see gray shading in bottom panel of Fig. 12). In this scenario, the periods of low-amplitude oscillations would correspond to the zones of low radar power defining the base of the radar units (i.e., the inter-packet zones), with the ice experiencing less sublimation—and thus less concentration of lithic materials—during the lower insolation peaks, thereby producing lower dielectric contrasts between successive deposits. At other times, each interval between the higher local maxima in the insolation function might then correspond to

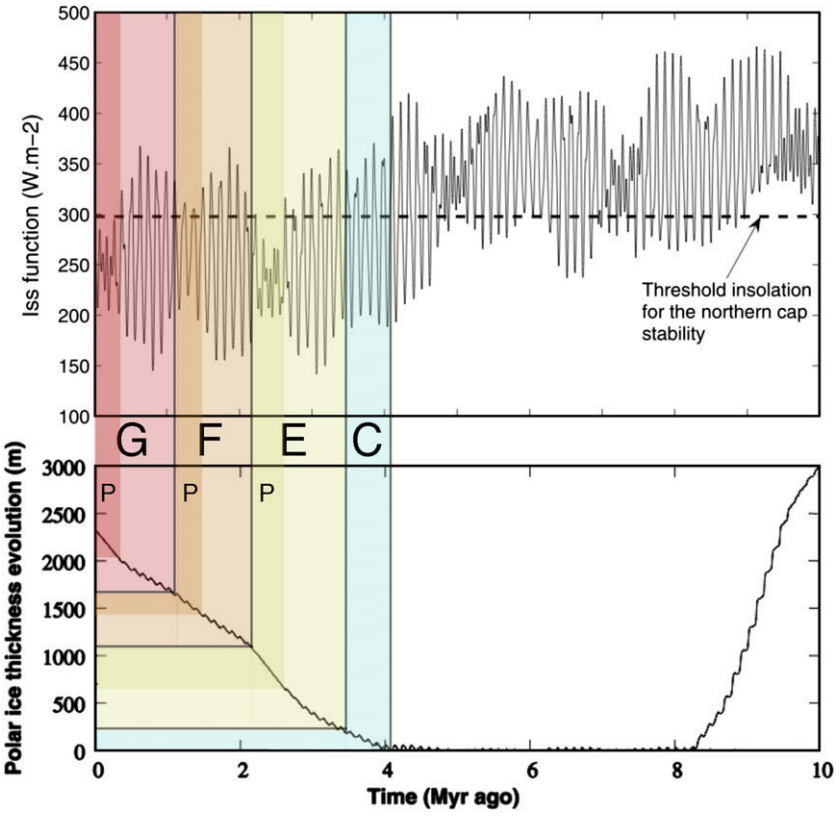

Fig. 11. Proposed correlation of radar Units C, E, F, and G with the summer-solstice insolation function and modeled polar-ice thickness of Levrard et al. (2007; their Figs. 3 and 4). Packets (P) of strong reflections in the radar, shown in darker shading of E–G, correspond to low-amplitude oscillations in insolation, and zones of weaker reflections (C, lighter shading of E–G) correspond to high-amplitude oscillations and short-period lows in insolation. See discussion in text.

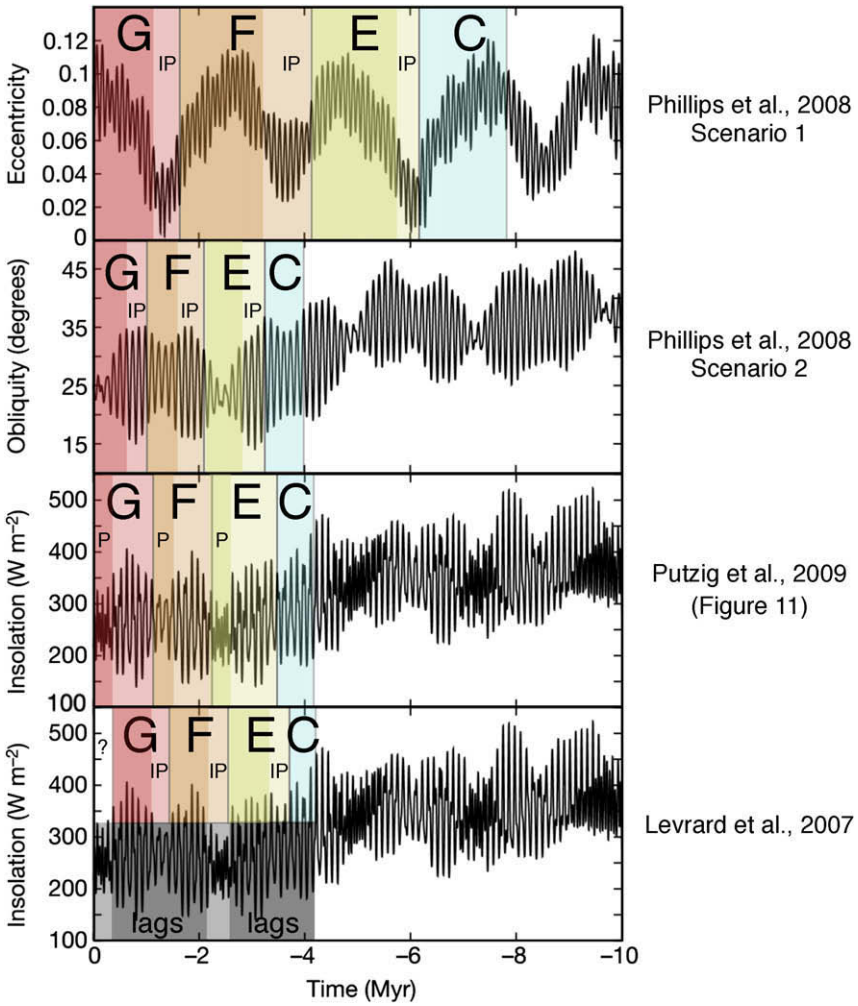

Fig. 12. Various correlations of radar Units C, E, F, and G with obliquity, eccentricity, and insolation functions of Laskar et al. (2002; their Fig. 2d–f). Levrard et al. (2007) predicted layering by lag formation during local insolation maxima (darker gray shading on bottom panel) and little or no lag forming when oscillations are suppressed (lighter gray shading), with the latter presumably leading to inter-packet zones (IP). However, no such zone appears to exist in the uppermost part of the NPLD. Phillips et al. (2008) suggested two alternative correlations, one in which inter-packet zones correspond to lows in eccentricity (top panel) and another where they correspond to short-period lows in obliquity (second panel). We modify their second scenario by correlating packet zones (P) to low-amplitude oscillations of insolation (third panel). See discussion in text.

individual radar-detected layers in the strongly reflective portions of the units (i.e., the packet zones) (see color shading in bottom panel of Fig. 12). The insolation function shows about 45 local maxima in the 4.2-Ma period, which appears to correspond closely to our estimate of 48 NPLD radar layers (Table 1). However, the fact remains that the most recent 300,000 years are a period of lower-amplitude oscillations in insolation and yet there is no zone of low radar power at the surface of the NPLD as might be expected, but rather a strongly reflective sequence. We therefore discount this scenario in favor of others that do not require formation of the inter-packet zones during periods with low-amplitude variations in insolation.

Considering these and other results, Phillips et al. (2008) suggested two other possible correlations between the SHARAD packet–inter-packet sequences and climate forcing due to orbital characteristics (upper two panels of Fig. 12). In the first scenario, the inter-packet zones correspond to lows in the 2.4-Myr cycle of eccentricity at ~1.4, ~3.8, and ~6.2 Ma (Laskar et al., 2002) and represent accumulation of ice with little dust, consistent with the expectation of low dust-storm activity at times of low obliquity and eccentricity (Toon et al., 1980). Meanwhile, the packets form during high obliquity when more prevalent dust storms (Haberle et al., 2003) deliver lithic material to the polar region and concentrate it as lags during excursions in insolation (Levrard et al., 2007). In the second scenario, the inter-packet zones are correlated to phases of short-period minimum obliquity at ~0.8, ~2.0, and ~3.2 Ma when ice may be accumulating more rapidly at the poles (Levrard et al., 2007). The first scenario extends the age of the deposits to ~6.5–6.8 Ma, well before the excursion to low mean obliquity of the last ~5 Myr, a period which the models suggest are not compatible with large deposits of polar ice at or near the surface. The timing in the second scenario is more favorable, but it must contend with short-period excursions to higher obliquity during the inter-packet periods and secularly variable insolation during the periods of packet formation.

To address the latter issue, we modify the second scenario of Phillips et al. (2008) by confining the period of packet formation to the lows in the oscillation of the insolation function of Levrard et al. (2007), accepting their maximum age constraint for the NPLD of ~4.2 Ma (see color shading in Fig. 11). The dielectric contrasts between layers in the packet zones would then be driven by variations in dust content during ice accumulation rather than by the production of lags during sublimation, in keeping with the mechanism for layering preferred by Laskar et al. (2002). In this revised

scenario, the longer periods with high-amplitude oscillations of insolation correspond to the weakly reflective inter-packet zones at the base of the radar units. These periods still encompass the obliquity minima, but nevertheless remain more difficult to explain, as one might expect significant lag production leading to large dielectric contrasts during the short-period excursions to high insolation values. However, such may not be the case if sublimation processes are less efficient than predicted or eolian activity removes any lag materials prior to the return to accumulation of relatively clean ice at low obliquity. Experiments with an atmospheric general circulation model (Haberle et al., 2003) suggest that, during times of high obliquity, atmospheric dynamics are favorable for lifting dust at high latitudes.

With regard to the higher age estimates, Tanaka et al. (2009) suggest a correspondence between the high obliquity period prior to ~4.5 Ma and an unconformity near the top of the NPLD that is too shallow to be resolved by SHARAD. In this scenario, nearly all of the radar-detected layers pre-date the precisely established obliquity history (unconstrained prior to ~10–20 Ma; see Laskar et al., 2004) and no correlation of insolation history to the bulk of NPLD layering is possible. Nevertheless, the cyclic and relatively conformal nature of the radar-detected layering could still be useful for constraining possible obliquity histories at earlier times. For example, if it can be shown by other means that the layering is likely to have been emplaced in the last few 100 Ma and not earlier, then those orbital solutions that retain high obliquity over extended periods of time prior to the 4.5-Ma transition can be discounted (e.g., 250-Ma obliquity histories in panels 1, 2, 10, 11, 13, and 15 in Fig. 11 of Laskar et al., 2004, would be more likely than the others).

In the absence of more definitive information, we cannot rule out the possibility that the NPLD layering is a function of much longer or shorter climate cycles (e.g., Tanaka, 2005) or even other, potentially chaotic processes that are not linearly related to orbital cycles (e.g., Perron and Huybers, 2009). The age of the NPLD might then be substantially younger or older than the ~4.2 Ma suggested here. To the degree that the insolation models are robust, a dramatically greater age will require some mechanism to protect the deposits from entirely sublimating away. A simple means of preservation is the production of thick lag deposits to preserve the ice through extended periods of high insolation. However, the fact that SHARAD obtains strong reflections through to the base of the NPLD stack limits the present-day lithic fraction to no more than several percent (Picardi et al., 2005; Nunes and Phillips, 2006; Phillips et al., 2008), and the relatively uniform and conformal nature of the layering in the inter-trough regions of the NPLD suggests that the deposits have not been subjected to widespread erosion over long periods of time. In contrast, the south polar layered deposits (SPLD)—which have substantially older surface cratering ages of 10–100 Ma (Herkenhoff and Plaut, 2000)—exhibit much more variable radar reflectivity, including apparent internal and near-surface angular unconformities suggestive of more widespread erosion (Plaut et al., 2007; Seu et al., 2007a; Milkovich et al., 2009; Phillips et al., 2009). These radar results are consistent with the identification of several local and regional unconformities within the SPLD on the basis of surface imagery and elevation data (Kolb and Tanaka, 2006, 2009).

6. Conclusions

The mapping work described here represents the first detailed examination of the internal structure of Planum Boreum that incorporates radar soundings. While the radar results generally confirm expectations of the internal structure that have been developing over decades of studying images and other surface data from the periphery and troughs where the layers outcrop (e.g., Clifford et al., 2000; Tanaka et al., 2008), they also provide a substantially more detailed view of that structure and reveal many new features. The unveiling by radar sounding of the basal unit's true geographic extent—present in Gemina Lingula and absent in the eastern main lobe—and of its subsurface topography—a generally dome-like structure, with an anomalous elongated peak beneath the western main lobe—raises interesting new questions about the history of these deposits and their influence on the subsequent evolution of the NPLD. A wedge of layers discovered in eastern Gemina Lingula hints at a dramatic shift in the north-polar ice depocenter early in NPLD history, attended by a restricted area of deposition. The periodic nature of the layers and packets of layers seen in the radar data provides a tantalizing new piece to the puzzle of the age of the NPLD. Constrained by clear evidence of surface-conformal, strongly reflective layers in the upper few hundred meters of the NPLD, we have proposed a seemingly counterintuitive correlation between the radar layering pattern and modeled cycles of insolation over the past five million years. We expect that more rigorous testing of this idea will supply fresh insights.

The advent of this rich dataset sheds new light on several important and long-standing mysteries and simultaneously opens a host of intriguing new avenues for investigation. Our mapping of the NPLD base confirms that it is extremely flat beneath Gemina Lingula and the eastern main lobe (Fig. 10), implying an extraordinary lack of significant isostatic compensation as discussed by Phillips et al. (2008). This result has far-reaching ramifications for regional and global heat flow and the nature of Martian mantle materials, which in turn impact a host of studies concerning crustal evolution, tectonics, and the distribution of liquid water and ice in the subsurface. Our choice of radar units within the NPLD was based on the packet–inter-packet sequences, whose cyclic patterns are suggestive of climatological processes, and we anticipate that important revelations about the climate history of Mars will be realized. Mapping of these units provides important new constraints on the internal structure of the NPLD, but other approaches such as unconformity-based mapping (e.g., Holt and Safaeinili, 2009) will add crucial details to the investigation of these deposits. While the troughs and surface undulations obscure our view of the subsurface in many areas by introducing unwanted clutter into the radar data, they are an integral part of the NPLD and have provided a window into the interior for image-based studies (e.g., Rodriguez et al., 2009). In some areas, the radar exposes structural features beneath the troughs and surface undulations (e.g., Fig. 2), and mapping of these features promises to impart key information about trough migration and development (e.g., Smith et al., 2009). An important next step in all of these investigations is the synthesis of the radar products with a host of other data sets and modeling results, which taken together will provide an impressive set of tools for unraveling the geology of Planum Boreum and Mars' climate history.

Acknowledgments

The Shallow Radar (SHARAD) instrument was provided to NASA's Mars Reconnaissance Orbiter (MRO) mission by the Italian Space Agency (ASI), and its operations are led by the InfoCom Department, University of Rome "La Sapienza." Thales Alenia Space Italia is the prime contractor for SHARAD. The MRO mission is managed by the Jet Propulsion Laboratory, California Institute of Technology, for the NASA Science Mission Directorate, Washington, DC. Lockheed Martin Space Systems, Denver, CO, is the prime contractor for the orbiter. We are grateful to all the people at these institutions who are instrumental in the ongoing success of the SHARAD experiment. We thank Prateek Choudhary and Isaac

Smith for providing simulated radargrams and helpful discussion of surface clutter features. We also thank Doug Paul, Kerry Befus, Ed VanWieren, and Ed Chow of SeisWare International Inc. for access to and support of the SeisWare interpretation software, which serves an integral role in our mapping efforts. Reviews by Ken Tanaka, Brian Davis, and an anonymous reviewer greatly improved the manuscript.

In dedicating this work to the late Dr. Ali Safaeinili, we wish to salute our friend and colleague for his outstanding contributions to the field of planetary radar science. His technical expertise, insightful analysis, and ability to catalyze international teamwork will continue to serve as an inspiration to all who knew him.

References

Byrne, S., Murray, B.C., 2002. North polar stratigraphy and the paleo-erg of Mars. J. Geophys. Res. 107, 5044, 12 pp. doi:10.1029/2001JE001615.

Clifford, S.M., and 52 colleagues, 2000. The state and future of Mars polar science and exploration. Icarus 144, 210–242.

Fishbaugh, K.E., Head, J.W., 2005. Origin and characteristics of the Mars north polar basal unit and implications for polar geologic history. Icarus 174, 444–474.

Grima, C., Kofman, W., Mouginot, J., Phillips, R.J., Hérique, A., Biccari, D., Seu, R., Cutigni, M., 2009. North polar deposits of Mars: Extreme purity of the water ice. Geophys. Res. Lett. 36, L03203, 4 pp. doi:10.1029/2008GL036236.

Haberle, R.M., Murphy, J.R., Schaeffer, J., 2003. Orbital change experiments with a Mars general circulation model. Icarus 161, 66–89.

Herkenhoff, K.E., Byrne, S., Russell, P.S., Fishbaugh, K.E., McEwen, A.S., 2007. Meter-scale morphology of the north polar region of Mars. Science 317, 1711–1715.

Herkenhoff, K.E., Plaut, J.J., 2000. Surface ages and resurfacing rates of the polar layered deposits on Mars. Icarus 144, 243–253.

Holt, J.W., Peters, M.E., Kempf, S.D., Morse, D.L., Blankenship, D.D., 2006. Echo source discrimination in single-pass airborne radar sounding data from the Dry Valleys, Antarctica: Implications for orbital sounding of Mars. J. Geophys. Res. 111, E06S24, 13 pp. doi:10.1029/2005JE002525.

Holt, J.W., and Safaeinili, A., 2009. Northern polar layered deposits, Mars: Structural relationships between Gemina Lingula, the main lobe, and Chasma Boreale from SHARAD radar stratigraphy. Lunar Planet. Sci. XL, 1721 (abstract).

Holt, J.W., Safaeinili, A., Plaut, J.J., Head, J.W., Phillips, R.J., Seu, R., Kempf, S.D., Choudhary, P., Young, D.A., Putzig, N.E., 2008. Radar sounding evidence for buried glaciers in the southern mid-latitudes of Mars. Science 322, 1235–1238.

Johari, G.P., 1976. The dielectric properties of H_2O and D_2O ice Ih at MHz frequencies. J. Chem. Phys. 64, 3998–4005.

Kolb, E.J., Tanaka, K.L., 2006. Accumulation and erosion of south polar layered deposits in the Promethei Lingula region, Planum Australe. Mars 2, 1–9.

Kolb, E.J., and Tanaka, K.L., 2009. Bed structures of polar layered deposit outcrops in Australe Mensa: Implications for the formational history of Planum Australe, Mars. Lunar Planet. Sci. XL, 2230 (abstract).

Laskar, J., Correia, A.C.M., Gastineau, M., Joutel, F., Levrard, B., Robutel, P., 2004. Long term evolution and chaotic diffusion of the insolation quantities of Mars. Icarus 170, 343–364.

Laskar, J., Levrard, B., Mustard, J.F., 2002. Orbital forcing of the martian polar layered deposits. Nature 419, 375–377.

Levrard, B., Forget, F., Montmessin, F., Laskar, J., 2007. Recent formation and evolution of northern martian polar layered deposits as inferred from a Global Climate Model. J. Geophys. Res. 112, E06012, 18 pp. doi:10.1029/2006JE002772.

Mätzler, C., Wegmüller, U., 1987. Dielectric properties of fresh-water ice at microwave frequencies. J. Phys. D: Appl. Phys. 20, 1623–1630.

Milkovich, S.M., Head, J.W., 2005. North polar cap of Mars: Polar layered deposit characterization and identification of a fundamental climate signal. J. Geophys. Res. 110, E01005, 21 pp. doi:10.1029/2004JE002349.

Milkovich, S.M., Plaut, J.J., Safaeinili, A., Picardi, G., Seu, R., Phillips, R.J., 2009. Stratigraphy of Promethei Lingula, south polar layered deposits, Mars, in radar and imaging data sets. J. Geophys. Res. 114, E03002, 21 pp. doi:10.1029/2008JE003162.

Morse, D.L., Waddington, E.D., Steig, E.J., 1998. Ice age storm trajectories inferred from radar stratigraphy at Taylor Dome Antarctica. Geophys. Res. Lett. 25, 3383–3386.

Nunes, D.C., Phillips, R.J., 2006. Radar subsurface mapping of the polar layered deposits on Mars. J. Geophys. Res. 111, E06S21, 16 pp. doi:10.1029/2005JE002609.

Perron, J.T., Huybers, P., 2009. Is there an orbital signal in the polar layered deposits of Mars? Geology 37, 155–158.

Phillips, R.J., and 13 colleagues, 2009. Subsurface structure of the south polar layered deposits, Mars. Lunar Planet. Sci. XL, 2007 (abstract).

Phillips, R.J., and 26 colleagues, 2008. Mars north polar deposits: Stratigraphy, age, and geodynamical response. Science 320, 1182–1185.

Picardi, G., and 33 colleagues, 2005. Radar soundings of the subsurface of Mars. Science 310, 1925–1928.

Plaut, J.J., and 33 colleagues, 2007. Subsurface radar sounding of the south polar layered deposits of Mars. Science 316, 92–95.

Plaut, J.J., Safaeinili, A., Holt, J.W., Phillips, R.J., Head III, J.W., Seu, R., Putzig, N.E., Frigeri, A., 2009. Radar evidence for ice in lobate debris aprons in the mid-northern latitudes of Mars. Geophys. Res. Lett. 36, L02203, 4 pp. doi:10.1029/2008GL036379.

Rodriguez, J.A.P., Tanaka, K.L., and Berman, D.C., 2009. Depression systems in Western Planum Boreum, Mars: Distributions, orientations, and cross-cutting relationships. Lunar Planet. Sci. XL, 2371 (abstract).

Selvans, M.M., Aharonson, O., Plaut, J.J., Safaeinili, A., 2009. Structure of the basal unit of the north polar Plateau of Mars, from MARSIS. Proc. IEEE Radar Conf., 3206 (abstract).

Seu, R., and 51 colleagues, 2007a. Accumulation and erosion of Mars' south polar layered deposits. Science 317, 1715–1718.

Seu, R., and 11 colleagues, 2007b. SHARAD sounding radar on the Mars reconnaissance orbiter. J. Geophys. Res. 112, E05S05, 18 pp. doi:10.1029/2006JE002745.

Smith, D.E., Frey, H.V., Carvin, J.B., Zwally, H.J., Lemoine, F.G., Rowlands, D.D., Abshire, J.B., Afzal, R.S., Sun, X., Zuber, M.T., 2001. Mars orbiter laser altimeter: Experiment summary after the first year of global mapping of Mars. J. Geophys. Res. 106, 23689–23722.

Smith, I.B., Holt, J.W., Christian, S.W., and Safaeinili, A., 2009. Evidence for spiral trough migration and evolution from SHARAD radar observations of stratigraphy within the northern polar layered deposits, Mars. Lunar Planet. Sci. XL, 1423 (abstract).

Tanaka, K.L., 2005. Geology and insolation-driven climatic history of Amazonian north polar materials on Mars. Nature 437, 991–994.

Tanaka, K.L., Rodriguez, J.A.P., Fortezzo, C.M., and Seelos, F., 2009. Obliquity-driven periods of extended erosion and deposition in the geologic record of Planum Boreum, Mars. Lunar Planet. Sci. XL, 2476 (abstract).

Tanaka, K.L., Rodriguez, J.A.P., Skinner, J.A., Bourke, M.C., Fortezzo, C.M., Herkenhoff, K.E., Kolb, E.J., Okubo, C.H., 2008. North polar region of Mars: Advances in stratigraphy, structure, and erosional modification. Icarus 196, 318–358.

Tanaka, K.L., Scott, D.H., 1987. Geologic map of the polar regions of Mars. USGS Miscellaneous Investigations Map I–1802–C.

Toon, O.B., Pollack, J.B., Ward, W., Burns, J.A., Bilski, K., 1980. The astronomical theory of climatic change on Mars. Icarus 44, 552–607.

Welch, B.C., Jacobel, R.W., 2003. Analysis of deep-penetrating radar surveys of West Antarctica, US-ITASE 2001. Geophys. Res. Lett. 30, 1444, 4 pp. doi:10.1029/2003GL017210.